DRAFT VERSION SEPTEMBER 16, 2010
Preprint typeset using LaTeX style emulateapj v. 04/20/08

FIRST CONSTRAINTS ON THE METALLICITIES OF HIGH-REDSHIFT LYMAN ALPHA GALAXIES[1]

STEVEN L. FINKELSTEIN[2,*], KARL GEBHARDT[3], GARY J. HILL[3], JOSHUA ADAMS[3], GUILLERMO A. BLANC[3], CASEY PAPOVICH[2]

Draft version September 16, 2010

ABSTRACT

We present the results of Keck/NIRSPEC spectroscopic observations of two Lyα emitting galaxies (LAEs) at $z = 2.3$ and 2.5 discovered with the HETDEX pilot survey. We detect Hα, [O III], and Hβ emission, representing the first detection of multiple rest-frame optical emission lines in high-redshift LAEs. We find that the systemic redshifts of these galaxies are different from that of the Lyα emission by 155 ± 37 and 81 ± 35 km s^{-1}, implying a significant large-scale outflow is occurring in the interstellar medium of at least one galaxy. This outflow is likely powered by star-formation activity, as examining these LAEs in a line-ratio diagnostic plane implies that neither hosts an active galactic nucleus. We place the first meaningful constraints on the gas-phase metallicities in LAEs by using the upper limits on the [N II] emission, finding $Z < 0.17$ and < 0.28 $Z_{\odot}$ in these two LAEs. Measuring the stellar masses of these objects ($\sim 10^{10}$ and 2×10^{8} M$_{\odot}$, respectively), we study the nature of LAEs in a mass-metallicity plane. These LAEs appear to be more metal poor than Lyman Break galaxies at the same redshift, implying that objects exhibiting Lyα emission may be systematically less chemically enriched than the general galaxy population at similar redshifts. Lastly, neglecting the contribution of the measured emission line fluxes when fitting models to the observed photometry can result in overestimates of the stellar population age by orders of magnitude, and stellar mass by a factor of ~ 3. This is particularly important at very high redshift, where similarly strong emission lines may masquerade in the photometry as a 4000 Å break.

Subject headings: galaxies: evolution

1. INTRODUCTION

Star-forming galaxies at high-redshift are one of the most useful probes of the distant universe. By studying their physical properties, we learn about the stellar mass, dust and chemical evolution of the first few Gyr after the Big Bang. The most efficient method of learning these properties is by comparing the observed colors of galaxies (their spectral energy distributions; SEDs) to model stellar populations, finding which combination of metallicity, star formation history, extinction, age and stellar mass best matches the observed galaxies (e.g., Papovich et al. 2001; Shapley et al. 2001; Bruzual & Charlot 2003, OTHER EARLY SED-FITTING PAPERS?). This requires only broadband photometry, thus many galaxies can be studied with a single dataset.

This technique has been used to study thousands of galaxies at high redshift, the majority of which are either color selected (Lyman break galaxies; LBGs; Steidel & Hamilton 1993), or selected on the basis of a bright Lyα emission line (Lyα emitters; LAEs; e.g., Cowie & Hu 1998; Rhoads et al. 2000). Over $3 < z < 6$, LBGs have been found to be highly star-forming galaxies (star-formation rate $\sim$ 10's of M$_{\odot}$ yr^{-1}), with significant dust attenuation (A$_V \sim 0.2$ - 1.0 mag), stellar population ages of 100's of Myr and stellar masses of $\sim 10^{10} - 10^{11}$ $M_{\odot}$ (e.g., Sawicki & Yee 1998; Papovich et al. 2001; Shapley et al. 2001, 2005; Yan et al. 2005, 2006; Eyles et al. 2005, 2007; Fontana et al. 2006; Reddy et al. 2006; Huang et al. 2007; Overzier et al. 2009; Stark et al. 2009).

Over the same redshift range, LAEs have been found to be less evolved in the same characteristics. Their star-formation rates are typically more modest ($< 10\,M_{\odot}$), they show zero or only modest dust extinction, they typically have ages < 100 Myr, and similarly masses of $\lesssim 10^{9}$ $M_{\odot}$ (e.g., Gawiser et al. 2006; Pirzkal et al. 2007; Finkelstein et al. 2007, 2008, 2009c; Gronwall et al. 2007; Lai et al. 2007, 2008; Pentericci et al. 2009; Ono et al. 2010b; Yuma et al. 2010).

Recent results imply that at $z \geq 7$ more evolved, LBG-like galaxies are rare, and that most galaxies have masses and ages similar to LAEs at $z < 6$ (e.g., Ouchi et al. 2009; Finkelstein et al. 2010b; González et al. 2010; Ono et al. 2010a). However, the samples studied thus far have been small, and further work is justified. While the physical properties of LBGs evolve from $z = 6 - 3$, the characteristics of LAEs appear unchanging, leading to the suggestion that they represent newly forming galaxies at each redshift (Malhotra et al., in prep), thus understanding the true characteristics of LAEs is highly interesting.

These analyses of the physical properties of LBGs and LAEs have all been based on the SED-fitting technique. While reasonably good at deriving well-constrained stellar masses, this technique only roughly constrains the dust extinction, and places no meaningful constraints on the metallicities in such galaxies. In order to learn about these crucial evolutionary properties in more detail, rest-frame optical spectroscopy is needed. However, at such high redshifts, these lines are shifted into the near-infrared, and thus are observationally challenging.

Erb et al. (2006) performed a large near-infrared spectroscopic survey of LBGs at $z \sim 2.3$ using the Keck telescope with the near-infrared spectrograph NIRSPEC (McLean et al. 1998). They primarily observed with a K-band filter, which allowed them to observe Hα and [N II] emission at this red-

[1] The data presented herein were obtained at the W.M. Keck Observatory from telescope time allocated to the National Aeronautics and Space Administration through the agency's scientific partnership with the California Institute of Technology and the University of California. The Observatory was made possible by the generous financial support of the W.M. Keck Foundation.

[2] George P. and Cynthia Woods Mitchell Institute for Fundamental Physics and Astronomy,
Department of Physics and Astronomy, Texas A&M University, College Station, TX 77843
[3] Department of Astronomy, University of Texas, Austin, TX 78712
[*] stevenf@physics.tamu.edu

shift (though they obtained H-band spectroscopy, and thus Hβ and [O III] measurements for a few objects). From the ratio of these lines, they derived the gas-phase metallicity of these objects. Combining them with stellar mass estimates, they examined the mass-metallicity relationship at z $\sim$ 2.3, finding that LBGs at that redshift followed a similar sequence of higher metallicity with higher mass as at very low redshift (Tremonti et al. 2004), though the sequence was shifted down by $\sim$ 0.5 dex in metallicity, showing that high-redshift LBGs are less chemically evolved than local star-forming galaxies. A number of other studies have taken advantage of magnification due to gravitational lensing to study high-redshift LBG-like galaxies in detail (e.g., Teplitz et al. 2000; Finkelstein et al. 2009b). However, until now, galaxies selected on the basis of Lyα emission have not been probed in physical detail.

LAEs are typically much fainter than LBGs, thus their emission line fluxes are fainter as well, resulting in more time-demanding observations. Recently, McLinden et al. (2010) published the first rest-frame optical emission line detections from LAEs, detecting [O III] emission from two LAEs at z $\sim$ 3.1. They were able to probe the kinematics of the ISM by comparing the redshifts of these lines to that of Lyα, finding that both galaxies exhibited large scale outflows. Additionally, Hayes et al. (2010) probed the Lyα escape fraction in high-redshift star-forming galaxies by measuring the Lyα and Hα fluxes with an optical and near-infrared narrowband filter, though only a few objects were simultaneously detected in both lines. However, probing further into the physical characteristics of such galaxies requires more than a single rest-frame optical line. In this Paper, we present the first detections of multiple rest-frame optical emission lines from high-redshift LAEs, which we use to study in detail their physical properties. In §2, we discuss the selection of our LAE sample, and our near-infrared spectroscopic observations with Keck/NIRSPEC. In §3, we discuss our emission line measurements. In §4 we measure the systemic redshift and look for the existence of outflows in the ISM, in §5 we probe for AGN signatures and in §6 we place constraints on the dust extinction. In §7, we constrain the gas-phase metallicities of our LAEs, including studying them on a mass-metallicity plane. Lastly, in §8 we examine how the measured emission line fluxes can affect the SED fitting results. We assume H_0 = 70 km s^{-1} Mpc^{-1}, Ω_m = 0.3 and Ω_m = 0.7, and unless specified we use the AB magnitude system throughout (Oke & Gunn 1983).

2. DATA

2.1. *Sample Selection*

The Hobby Eberly Telescope Dark Energy Experiment (HETDEX) is a blind integral field unit (IFU) search for LAEs at z = 1.9 – 3.5, with a primary science goal of probing dark energy via baryonic acoustic oscillations. The survey will begin in 2011, using the Visible Integral-field Replicable Unit Spectrograph (VIRUS) instrument, which is composed of 150 individual IFUs (Hill et al. 2008). Currently, a single pilot IFU (VIRUS-P) is mounted on the 2.7m Harlan J. Smith Telescope at the McDonald Observatory. Over the past 4 years, VIRUS-P has been used for 111 nights as part of a HETDEX pilot survey, discovering 103 LAEs at z $\sim$ 2–3 (Adams et al. in prep; Blanc et al. in prep). These LAEs are at redshifts ripe for near-infrared spectroscopic follow-up.

We were granted one night on the Keck II 10m telescope with NIRSPEC to obtain near-infrared spectroscopy of HETDEX pilot survey LAEs. We selected LAEs from the pilot survey sample by requiring that the redshift be such that Hα was observable with NIRSPEC (i.e., $z_{Ly\alpha} \lesssim 2.7$) and that the Ly$\alpha$ line flux was greater than 10^{-16} erg s^{-1} cm^{-2}. The latter criterion ensured that Hα and Hβ should be bright enough to observe in 90 minutes with NIRSPEC (assuming the ratio of Lyα/Hα was $\sim$ 4). We selected $\sim$ 10 LAEs in this manner, and chose three for observation on this run – two in the COSMOS field, and one in the Hubble Deep Field North (HDFN), named COSMOS_156, COSMOS_104 and HDFN_146, respectively, where the numbers correspond to the index in the HETDEX pilot survey catalog (Adams et al., in prep). These three LAEs have Lyα-based redshifts of 2.2889, 2.4914 and 2.2357 (Adams et al., in prep). More details on these LAEs are listed in Table 1.

2.2. *NIRSPEC Observations*

Our observations took place on UT 21 February 2010, and conditions were photometric throughout the night. We observed in low–resolution spectroscopy mode, with a slit width of 0.76″(and the standard slit length of 42″). Throughout the night, the cross disperser was kept at 35.76º. When using the NIRSPEC–7 filter (hereafter referred to as the K–band), this resulted in a wavelength coverage of 2.02 – 2.43 μm, while with the NIRSPEC–5 filter (hereafter referred to as the H–band), this provided a wavelength coverage of 1.48 – 1.76 μm.

We observed all three LAEs for 90 minutes in the K–band filter, obtaining 6 $\times$ 15-minute exposures. We also observed COSMOS_156 for 90 minutes (6 $\times$ 15-minutes) in the H–band, while we only obtained 20 minutes (2 $\times$ 10 minutes) in the H–band on COSMOS_104 due to time constraints. The science spectroscopic observations were taken in an ABBAAB pattern. Telluric standards were observed before and after each observing setup in an ABBA pattern, where we selected stars from the Hipparcos survey catalog with a spectral type near F0V, which minimizes hydrogen absorption lines common in early–type stars, and metallic lines common in later–type stars. In addition, we obtained arc lamp calibration images between each observing setup, as the wavelength solution may drift throughout the night. NIRSPEC is known to have significant persistence when the integrated counts pass $\sim 10^4$ per pixel. During the afternoon, we examined the decay of this persistence by taking dark frames, and we found it to disappear on timescales of $\sim$ 15 minutes. However, as a precaution, we varied the position on the slit of both our objects and our standard stars, such that adjacent exposures should not have science data falling on the same pixel rows.

Our targets were acquired using the "invisible acquisition" mode of NIRSPEC. In this mode, an alignment star must be placed in the slit simultaneously with the object, and the star must have $K_{Vega} \lesssim 18$ to be useful. We found alignment stars of K_{Vega} = 16.5, 17.0 and 18.0 at distances of 26″, 17″ and 31″ from COSMOS_156, COSMOS_104 and HDFN_146, respectively. We first acquired the star at the center of the slit, then we slid the star toward one end of the slit, such that the star and the target LAE were equidistant from slit center. During an exposure, we actively guided the slit using the slit–viewing camera (SCAM), which continuously images the same field of view as the spectrograph, excepting the light which is transmitted down the slit. Throughout the night our seeing was steady at 0.6 – 0.9″, comparable to the size of the

TABLE 1
SUMMARY OF NIRSPEC-TARGETED LAES

Object	RA (J2000)	Dec (J2000)	$F_{Ly\alpha}$ (10^{-17} erg s^{-1} cm^{-2})	$EW_{Ly\alpha}$ (Å)	λ_{obs} (Lyα)	λ_{corr} (Lyα)	$z_{Ly\alpha}$
COSMOS_156	150.05908	2.240587	61.0 ± 4.2	120.3 ± 23.2	3998.0	3998.2	2.2889 ± 0.0004
COSMOS_104	150.11805	2.299566	31.4 ± 4.5	308.7 ± 123.6	4244.1	4244.4	2.4914 ± 0.0004
HDFN_146	189.20890	62.233631	24.5 ± 3.1	83.3 ± 29.5	3933.6	3933.5	2.2357 ± 0.0004

NOTE. — The equatorial coordinates provided correspond to the optical counterpart to the Lyα emission which were used as the NIRSPEC targets. The detections of rest-frame optical emission lines at the expected wavelengths confirm these counterparts as correct (with the possible exception of HDFN_146). The computed redshifts include a heliocentric correction to correct for the Earth's motion. The error on the redshift reflects a typical uncertainty on the central wavelength of the Lyα line of 0.5 Å, which dominates over the typical wavelength solution error of 0.05 Å.

slit, thus when the star was well centered, only the wings of the PSF were visible to either side of the slit. If the star started to drift out of the slit, we manually moved the slit to keep pace, using 0.5 pixel increments ($\sim 0.09''$), ensuring that our object stayed centered in the slit throughout each exposure.

2.3. *Data Reduction*

We used a combination of the Keck IDL–based REDSPEC[1] package along with our own custom IDL scripts to reduce the data. Using REDSPEC for the initial steps, we reduced each object/filter combination separately. For each combination, we used calibrations taken the closest in time, consisting of four calibration star spectra (in an ABBA pattern) and two arc lamp images (one neon and one argon). As the flat field is not expected to vary during the night, we used flat fields taken during the afternoon for calibration. On each combination, we first ran the REDSPEC task `spatmap`, which uses the standard star spectra to compute a spatial map of the image, allowing rectification to be performed. The task `specmap` was then run, which computes the wavelength solution, where the lines are marked interactively via a GUI. Finally, the task `redspec` was run, which rectifies and extracts the spectra. However, as our objects are so faint that their continuum light is not visible, the redspec extraction was not satisfactory. Thus, we ran `redspec` to obtain the wavelength–pixel solution, but we ran the REDSPEC task `rectify` to separately rectify the science images without extraction.

We rejected cosmic rays from our rectified spectra (both science and calibration) using the LACOSMIC package (van Dokkum 2001). These images were then sky subtracted by subtracting adjacent image pairs, with one each in the A and B dither position, where the object was dithered by $5''$ between frames (with the exception of HDFN_146, where the dither was only $3''$ in order to keep the alignment star in the slit). We then removed residual sky lines from these sky subtracted images by fitting and subtracting a 15th order polynomial to each image column, where the positive and negative target and alignment star spectra were masked out during the fitting.

The 1D spectral extraction was performed by reading each image into IDL, and extracting a 2D rectangular box centered on the spectra. The box was chosen to be 9 pixels wide, corresponding to $1.7''$, or $\sim$ 2X the average seeing. The same box size was used for both the target LAEs as well as the standard stars. During this process, the extraction region was centered based on the Hα or [O III] λ5007 emission lines, which were visible in the individual K– or H–band exposures. We also verified the wavelength solution during this process to find and correct any relative shifts between the exposures. These boxes were then summed column by column to create a 1D spectrum for each observation. We averaged the individual 1D spectra to create the final 1D spectra. This procedure was repeated for each science and standard star observation[2].

While we were able to make 1D spectra for COSMOS_156 and COSMOS_104, we were not able to detect Hα in individual frames for HDFN_146. Given the positive detection of Hα emission in the other two LAEs, we would have expected a detection here. However, the alignment star used with HDFN_146 was very faint, with K_{Vega} = 18, thus we required 180 s SCAM integrations to see the star. Given the level of slit shift seen in the other objects with much shorter SCAM exposures, we believe that it is likely that HDFN_146 drifted out of the slit multiple times, which resulted in the non-detection. Future observations of very faint targets are advised to use brighter alignment stars ($K_{Vega} \leq 17$) to avoid this issue. Thus for the remainder of the paper, we focus on COSMOS_156 and COSMOS_104, which have positive emission line detections.

The spectra of these two LAEs were corrected for Telluric absorption as well as flux calibrated using the standard star spectra. This was done by taking a **?** model star spectrum of the same spectral type of the standard, and normalizing its flux such that the H or K–band magnitude of the model matched that of the standard, where the photometry of the standard was obtained from the Two Micron All Sky Survey (2MASS) Point Source Catalog. We computed a calibration array by taking the ratio of the normalized model spectrum to the observed standard spectrum, interpolating over absorption features common to both spectra. This calibration array was multiplied into the observed object spectrum, both flux calibrating, and correcting for Telluric absorption. In addition, as our targets are unresolved from the ground, this calibration also corrects for point–source slit losses, as the standard and object had the same spectral extraction size, and the standard spectrum was normalized to match the total magnitude for that star.

A noise spectrum was created for each exposure for each object. This was done by first extracting a series regions of the same size as used on the object, starting at the bottom of the 2D spectrum, and moving successively up by 9 rows at a time (i.e., so that no two rows are included in more than one

[1] http://www2.keck.hawaii.edu/inst/nirspec/redspec.html

[2] For both K–band observations and the H–band observation for COSMOS_104, one standard spectra was significantly deviant from the other three observations; however the deviant spectrum was excluded from the analysis by the use of a median average.

noise estimate) in every input image, providing a 1D spectrum for each of the extracted rows. The noise in each spectral pixel was thus obtained by fitting a Gaussian to the pixel values in each column, performing two sigma clipping iterations (at 3 σ) to reject any real objects, and then measuring the standard deviation. This process created a 1D error spectrum for each image. These were then added in quadrature, and divided by the number of input frames (i.e., error propogation of a mean) to create a final 1D error spectrum for each object. Although this spectrum provides a good approximation of the photometric error at each wavelength, it does not include uncertainties on the flux calibration, which are important as some of the physical quantities which we wish to calculate rely on ratios between the two filters we have observed. To include this effect, during the extraction of the standard star we computed a calibration error spectrum from the standard deviation of the standard star spectra in each wavelength bin. We found that the noise from this process was typically much less ($\lesssim$ 1%) than the photometric noise; nonetheless this error spectrum was then added in quadrature to the photometric error spectrum for each object to include the uncertainties in the calibration process in our final error spectrum.

3. EMISSION LINE MEASUREMENTS

Figure 1 and Figure 2 show the reduced and flux-calibrated 1D spectra for COSMOS_156 and COSMOS_104, respectively, with the 1D error spectra shown in the bottom of each panel. The left and right panels in each figure show the region of the spectra around Hβ and [O III] (left) and Hα and [N II] (right), using the measured redshift of Lyα to estimate the expected positions of these rest-frame optical lines. Investigating Figure 1, it is apparent we have detected Hα emission at high significance, while the small bump in the spectrum just to the right could be [N II] emission. In the left panel, both [O III] λ4959 and [O III] λ5007 are strongly detected. There also appears to be an emission line at the expected position of Hβ. The blue portion of this line coincided with a night sky line. However, the right portion is unaffected, and in fact one can see the red half of the Hβ emission line when examining the 2D spectra, thus we conclude it is real. In Figure 2, we again see a strong detection of Hα, though there is no positive feature at the expected position of [N II]. In the H-band spectra, we see possible emission lines at the expected positions of [O III] 4959, [O III] 5007 and Hβ, though it is difficult to tell if these lines are significant, given the large number of sky-line residuals present in the reduced spectra.

In order to quantify the detection significance of each of these emission lines, as well as to measure the properties of the emission lines, we fit a Gaussian curve to each detected line using the MPFIT IDL software package[3]. For the K-band spectra for both objects, we fit a double Gaussian around the position of the detected Hα flux, allowing it to fit one Gaussian to the Hα flux, and a second Gaussian to [N II]. We fit a 500 – 600 Å-wide region of the spectra to allow ample room for the estimation of the continuum. MPFIT requires as input an estimate of the fitted parameters, which are the continuum flux, line wavelength, line FWHM and line flux. These numbers were estimated from the 1D spectra.

As the [N II] line is either only weakly detected, or not detected at all, we forced the second Gaussian to have the same FWHM and redshift as the first Gaussian for both objects, thus the only free parameter for the [N II] line is the line flux. This was performed iteratively, by forcing the FWHM and redshift of the [N II] fit to be fixed to initially the same value as was estimated for Hα, and then in successive iterations forcing the [N II] parameters to be equal to the Hα FWHM and redshift from the previous iteration. This was done until the difference in redshift between the two lines was $\Delta z < 0.00001$ and the difference in the FWHM was ΔFWHM < 0.01. In addition, the flux of the [N II] line was constrained to be positive.

Similar Gaussians were fit to the H-band spectra for both objects. As these lines are more separated then Hα+[N II] we fit three separate Gaussians to the Hβ, [O III] λ4959, and [O III] λ5007 lines. For COSMOS-156, all line parameters for the two [O III] lines were free to vary. However, as a portion of the Hβ line was lost due to sky emission, we fixed the Hβ wavelength and FWHM to match that of the [O III] λ5007 line. The much greater noise on the blue half of the line ensures that the red half (where we see the significant flux) dominates the fit. For COSMOS_104, only the [O III] λ5007 line appears obviously above the sky noise. Thus, we fixed both the redshift and the FWHM of Hβ and [O III] λ4959 to match that of the [O III] λ5007 line during the fitting.

It is difficult to judge the detection significance of a given emission line simply by examining the spectra surrounding the line, as surrounding regions might be heavily affected by residual sky lines, while the line region itself might be relatively free. We thus quantified the uncertainties in the emission line fit parameters by running a series of 10^3 Monte Carlo simulations on each spectrum. For each simulation, each spectral element was varied by an amount randomly proportional to the flux error at that wavelength, using a Gaussian random number, with a distribution centered on zero with a standard deviation of 1. The altered spectrum then had its emission lines fit in the same way as was done on the actual data (i.e., holding the same parameters fixed which were with the data). Through these simulations, we thus compiled 10^3 estimates of the line wavelengths (and thus redshifts), FWHMs and fluxes. We computed the 1 σ uncertainty on these parameters as one half of the spread of the central 68% of these values. The simulation results are shown in Figure 1 and Figure 2 as the red shaded region, which shows the central 68% of the simulation fits, highlighting the 1 σ uncertainty on these fits.

In Table 2 we tabulate all of the measured emission line properties, as well as the uncertainties on these properties from our simulations. We find that [N II] is not significantly detected in either object. To confirm our original estimate of the 1 σ uncertainties on the [N II] line fluxes, we performed another set of simulations, where we input into the K-band spectra of each object mock emission lines of varying strengths. We then ran Monte Carlo simulations on each mock spectrum to assess the signal-to-noise of the mock emission line detection. Plotting the signal-to-noise versus the mock line flux, we fit a line to the data, where the slope of this line is the 1 σ flux limit. We found 1 σ limits on the [N II] flux of 1.47×10^{-18} and 1.75×10^{-18} erg s^{-1} cm^{-2} for COSMOS_156 and COSMOS_104, respectively. We use these limits in the following analysis. We find that we detect the remaining lines at > 5 σ significance, except [O III] λ4959 in COSMOS_104, which is detected at 3.7 σ significance. These detection significances roughly conform to what one would expect by eye when examining the 2D spectra in Figures 1 and 2.

4. RESULTS

[3] http://www.physics.wisc.edu/∼craigm/idl/fitting.html

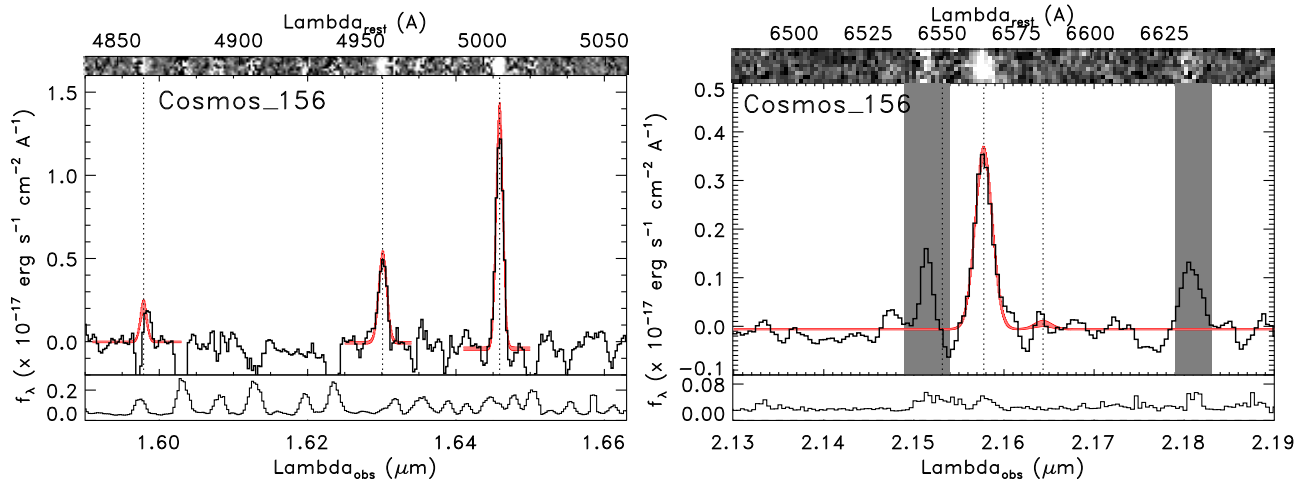

FIG. 1.— Left: H-band spectrum for COSMOS_156. The top panel shows the reduced two-dimensional spectrum. In the middle panel, the black line shows the observed 1D spectrum, smoothed to match the NIRSPEC resolution at these wavelengths. Based on the redshift of Lyα for this object, we easily identify both [O III] emission lines. We also identify Hβ emission, although the blue half of the line is affected by a sky line residual. The red shaded region denotes the 1 σ range of allowable fits to these emission lines. We fixed the redshift and FWHM of Hβ to match [O III] λ5007 to allow us to fit a Gaussian to half of a line. The bottom panel shows the 1D error spectrum, in the same units as the middle panel, magnified on the flux axis to show the structure of the noise. Right: K-band spectrum for COSMOS-156. While Hα is obviously strongly detected, [N II] only appears as a weak bump, and is not significant. Strong sky-line residuals are masked out behind the gray vertical bars.

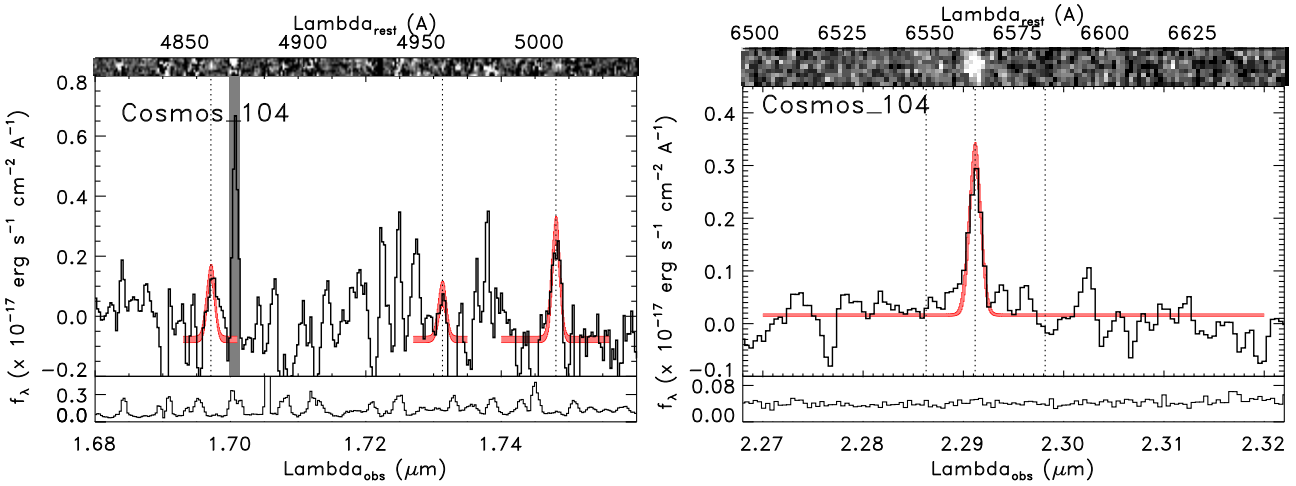

FIG. 2.— Left: H-band spectra for COSMOS_104, with the lines and shaded regions the same as in Figure 1. The redshift and FWHM of the [O III] λ4959 and Hβ lines were fixed to the value measured for [O III] λ5007. Our fits show that Hβ and [O III] λ5007 are detected, while [O III] λ4959 is not. Right: K-band spectrum for COSMOS_104. Although we do not see [N II] emission by eye, we still allow a Gaussian to be fit to its expected position to obtain an estimate of the upper limit on its line flux.

4.1. *Redshift and Outflows*

The simple fact that we detect Hα emission (along with Hβ and [O III]) near the expected wavelength confirms the original identification of our two objects as LAEs at $z \approx 2.3$ and 2.5. However, by comparing the exact values of the redshift derived from Lyα to that derived from the rest-frame optical emission lines, we can examine the kinematic state of the interstellar medium (ISM) in these galaxies. In many LBGs Lyα has been found to have a slightly higher redshift than the systemic redshift of the galaxy. Using a composite of $\sim$ 800 LBG UV spectra, Shapley et al. (2003) found that Lyα was redshifted by 360 km s^{-1} with respect to the systemic redshift. Additionally, the ISM absorption lines were blueshifted by –150 km s^{-1}. In an analysis of the gravitationally lensed z = 2.38 galaxy the Cosmic Horseshoe, Quider et al. (2009) resolved two separate Lyα emission peaks, each redshifted with respect to the systemic redshift, by 116 and 275 km s^{-1}, respectively, as well as measuring an average ISM absorption blueshift of –146 km s^{-1}. Lastly, Steidel et al. (2010) studied the ISM kinematics of a sample of 89 galaxies at $z \sim 2.3$, finding that Lyα and the ISM absorption lines were shifted by 445 and – 164 km s^{-1}, respectively, when compared to the systemic redshift as measured by Hα emission.

These velocity differences are thought to be due to the presence of global outflows in the ISMs of these galaxies. In such a situation, the non-resonant nebular lines are observed at the systemic redshift, as they originate from the H II regions within the galaxy. The ISM absorption lines are seen as blueshifted with respect the systemic redshift, as the absorption features are created when the outflowing gas on the

TABLE 2
MEASURED EMISSION LINE PROPERTIES

Object	Line	λ_{rest} (Å)	λ_{obs} (Å)	λ_{corr} (Å)	z	F_{line} (10^{-17} erg s^{-1} cm^{-2})	EW_{rest} (Å)
COSMOS–156	Hβ	4861	15978.9 ± 0.2	15978.4	—†	2.44 ± 0.43	33 ± 6
COSMOS–156	[O III]	4959	16301.2 ± 0.3	16300.7	2.28710 ± 0.00006	7.30 ± 0.42	84 ± 5
COSMOS–156	[O III]	5007	16458.8 ± 0.2	16458.3	2.28706 ± 0.00003	16.2 ± 0.5	196 ± 6
COSMOS–156	Hα	6563	21577.6 ± 0.4	21577.0	2.28767 ± 0.00005	8.80 ± 0.29	186 ± 6
COSMOS–156	[N II]	6583	21643.4 ± 0.4	21642.8	—†	< 0.15	< 3
COSMOS–104	Hβ	4861	16971.1 ± 0.9	16970.6	—†	3.33 ± 0.42	—
COSMOS–104	[O III]	4959	17313.2 ± 0.9	17312.7	—†	2.24 ± 0.61	—
COSMOS–104	[O III]	5007	17480.8 ± 0.9	17480.3	2.49117 ± 0.00018	5.38 ± 0.57	—
COSMOS–104	Hα	6563	22911.7 ± 0.44	22911.0	2.49094 ± 0.00007	4.44 ± 0.28	—
COSMOS–104	[N II]	6583	22981.5 ± 0.44	22980.8	—†	< 0.18	—

NOTE. — †The redshifts for the [N II] lines for both objects were fixed to the value measured for Hα, thus we do not list a value for those redshifts. Similarly, the redshifts for Hβ in COSMOS_156, and Hβ and [O III] λ4959 for COSMOS–104 were fixed to the value measured for [O III] λ5007 for those objects. Both [N II] lines were detected at $< 3\ \sigma$ significance, thus we list the $1\ \sigma$ upper limits. Using the redshifts listed above, the weighted mean redshifts for COSMOS_156 and COSMOS_104 are $z = 2.28720 \pm 0.00003$ and $z = 2.49096 \pm 0.00006$, respectively. The equivalent widths were computed from the ratio of the observed line flux to that of the continuum flux near the line from the best-fit model. COSMOS_104 is not detected in the IRAC bands, thus the model continuum fluxes at those wavelengths and the EWs of the emission lines are unconstrained, so we do not list their EWs.

near side (with respect to the observer) absorbs stellar light. Lastly, Lyα preferentially escapes after it has back-scattered off of the far side of the expanding ISM, shifting the Lyα-line center out of resonance with H I, enabling it to traverse back across the galaxy, and through the near side of the ISM.

Although these outflows appear ubiquitous in LBGs, the data did not exist until recently to perform the same analysis for the typically less luminous population of LAEs. McLinden et al. (2010) recent probed for outflows in two $z \sim 3.1$ LAEs with [O III] emission line detections. They found that the Lyα emission lines in their galaxies were redshifted by 142 and 284 km s^{-1} with respect to the [O III] emission, which presumably hails from the systemic redshift. Although this is a small sample, the outflow velocities in these galaxies are smaller than those in LBGs. This could easily be explainable, as LBGs are more massive and form stars at a higher rate (e.g., Papovich et al. 2001; Shapley et al. 2001; Yan et al. 2005; Stark et al. 2009), which could explain the more intense outflows. However, a larger sample of LAE outflow velocities needs to be compiled before strong conclusions can be made.

With our emission line redshifts, we have the data necessary to probe the existence of outflows in our LAEs. However, the optical and NIR datasets were taken on different dates and at difference observatories. The relative motion of the Earth (both rotational and orbital) as well as the motion of the Sun with respect to the observed target will thus be slightly different for the two datasets. Thus, before we compare the redshifts of the emission lines, we need to correct the observed line wavelengths for this effect. We computed the necessary correction from the observed data to the local standard of rest using the online V_{LSR} calculator[4]. The optical spectra of COSMOS_156 and COSMOS_104 were obtained at McDonald Observatory on UT 2008-12-29 and 2008-11-29, respectively. Including the time of observation, we found that the radial velocity of the observer with respect to the target was −15.55 and −21.37 km s^{-1}, respectively. The NIR spectra of these two objects were obtained at the Keck Observatory on UT 2010-02-21. Similarly including the observation times, the radial velocity with respect to the target was 8.66 and 8.40 km s^{-1} for the COSMOS_156 H- and K-band spectra, and 9.09 and 8.94 km s^{-1} for the COSMOS_104 H- and K-band spectra, respectively. The sign of these measurements is such that a positive number means that the observer was moving away from the target (with respect to V_{LSR}) at the time of the observation, so the line would appear at a slightly higher redshift.

We used these corrections to corrected the observed emission line wavelengths in both datasets, and computed the redshifts of the lines, both of which are listed in Tables 1 and 2. For the NIR data, we only computed the redshift when it was a free parameter, as in both objects the redshift of [N II] was fixed to match that of Hα, and in COSMOS_104, the redshift of Hβ and [O III] λ4959 was fixed to match that of [O III] λ5007. We computed the systemic redshift of each galaxy using the weighted mean of all measured rest-frame optical emission line redshifts.

The systemic redshift for COSMOS_156, using Hα and both [O III] lines, is $z_{sys} = 2.28720 \pm 0.00003$. For COSMOS_104, using Hα and [O III] λ5007, it is $z_{sys} = 2.49096 \pm 0.00006$. The Ly$\alpha$ based redshift for these two galaxies is $z_{Ly\alpha} = 2.2889 \pm 0.0004$ and 2.4914 ± 0.0004, respectively. Comparing these two redshifts, we find that for COSMOS_156, $z_{Ly\alpha}$ is redshifted compared to z_{sys} by $\Delta v = 155 \pm 37$ km s^{-1}. Similarly for COSMOS_104, $z_{Ly\alpha}$ is redshifted compared to z_{sys} by $\Delta v = 81 \pm 35$ km s^{-1}. This implies that outflows are present in the ISMs of both galaxies, though the result for COSMOS_156 is more significant.

Compared to the outflows in LBGs, the measured outflows in our LAEs appear lesser in magnitude, similar to what was found in McLinden et al. (2010) for their two LAEs. While a sample of four objects is still not enough to make robust conclusions, it is intriguing that LAEs appear to have systematically smaller outflow velocities than LBGs. This could be do to any variety of physical effects, as we still do not truly understand the difference between these two populations of galaxies. However, in the literature, LAEs tend to be less luminous, lower in stellar mass, forming stars at a lesser rate, and living in smaller dark matter halos than LBGs (e.g., Pa-

[4] http://fuse.pha.jhu.edu/support/tools/vlsr.html

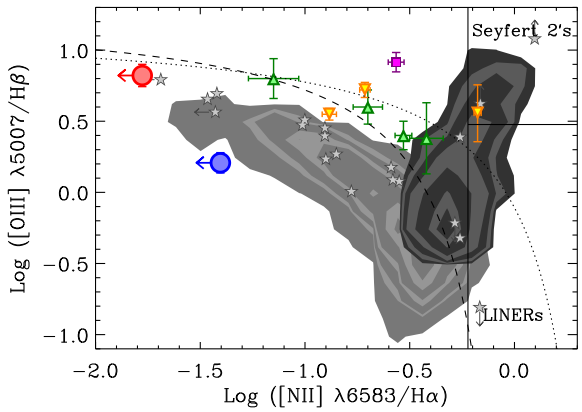

FIG. 3.— Our two LAEs are plotted on a BPT line-ratio diagnostic diagram, with COSMOS_156 in red, and COSMOS_104 in blue. The light and dark gray contoured regions denote where local star-forming and AGN-dominated galaxies lie, respectively, using data from the SDSS. The dotted line is the maximum starburst curve from Kewley et al. (2001), while the dashed curve is an updated SF/AGN demarcation line from Kauffmann et al. (2003). The solid lines denote regions expected to be inhabited by Seyfert 2's and LINERs (Kauffmann et al. 2003). Green triangles denote four $z \sim 2.3$ LBGs studied by Erb et al. (2006). The purple square is the position in this diagram of the z=2.73 lensed galaxy the 8 o'clock arc (Finkelstein et al. 2009b), while the yellow inverted triangles represent three $z \sim 2$ lensed galaxies studied by Hainline et al. (2009). The gray stars denote $z \sim 0.3$ LAE-analogs (Finkelstein et al. 2009a).

povich et al. 2001; Shapley et al. 2003; Gawiser et al. 2006, 2007; Pirzkal et al. 2007; Gronwall et al. 2007; Finkelstein et al. 2009c; Stark et al. 2009; Finkelstein et al. 2010b; Ono et al. 2010b). Steidel et al. (2010) analyzed their sample of $z \sim 2.3$ galaxies to discern if the outflow velocities they derived were correlated with any physical property, including those stated above. They found that the velocity difference between the systemic redshift and the interstellar absorption features and Lyα emission in their sample does not positively correlate with any of the physical properties. This is surprising, as it has been shown that the outflow speed can correlate with the star-formation rate (Martin 2005; Rupke et al. 2005). Steidel et al. (2010) did find that the velocity offset of the ISM absorption features anti-correlates with both the baryonic and dynamical masses (though at less than 3 σ), which could imply that the more massive galaxies are accreting inflowing material at the systemic velocity. Thus, it appears that more work is needed to probe the root physical cause of the outflows in high-redshift star-forming galaxies.

5. SIGNATURES OF ACTIVE GALACTIC NUCLEI

Although star formation can produce Lyα emission, active galactic nuclei (AGNs) also produce copious amounts of ionizing photons, and thus their host galaxies emit in Lyα as well. Understanding whether the production of Lyα photons is dominated by star formation or AGN activity is crucial in understanding not only the emission line, but also the characteristics of the galaxy as well. At high-redshift ($z > 3$), the only way to diagnose the presence of an AGN is via X-ray emission. Using deep X-ray observations, the AGN fractions of LAEs at $z > 3$ have been found to be typically 0 - 2 % (e.g., Malhotra et al. 2003; Wang et al. 2004; Gawiser et al. 2006; Ouchi et al. 2008). However, only the strongest AGNs will be detectable with currently available X-ray observatories.

At lower redshifts, the mid-infrared fluxes of galaxies can be used to diagnose the presence of AGNs, as they typically exhibit red power law slopes (Stern et al. 2005; **?**). Locally, AGNs have been identified using the line ratio diagram of Baldwin et al. (1981, hereafter BPT), which separates galaxies into star-forming and AGN sequences, independent of X-ray luminosity. This is done by plotting the ratio of [O III]/Hβ versus [N II]/Hα, where AGNs experience elevated levels on both ionized metal lines with respect to star-forming dominated galaxies. Finkelstein et al. (2009a) used this line diagnostic to study a sample of Lyα-emitting galaxies discovered with GALEX at $z \sim 0.3$ (Deharveng et al. 2008). They found that even though only 1 of their 23 galaxies exhibited detectable X-ray emission, 9 fell on or near the AGN sequence of the BPT diagram. While this may indicate that lower-redshift galaxies are more likely to host AGNs, it could also indicate that less luminous, or obscured, AGNs are lurking in LAEs at high redshift. This is especially critical at the redshifts of our LAE sample here, as they lie near to the redshift of peak AGN activity (e.g., **???**).

To study the possibility of AGN activity in our sample of LAEs, we first analyzed both the COSMOS *Chandra* Bright Source Catalog (v2.1 Puccetti et al. 2009) and the COSMOS XMM Point-like Source Catalog for X-ray counterparts near to our LAEs. In both catalogs, we found no X-ray counterparts within 10″ of our LAEs. We then plotted the positions of our two LAEs on a BPT diagram, shown in Figure 3. We denote the limits due to the upper limit on the [N II] fluxes by arrows. We plot contours of where objects from the Sloan Digital Sky Survey (SDSS) fall in this plane[5], with the AGN-dominated objects shown as the dark-gray contours, and the star-formation dominated objects shown as the light-gray contours. Both of our LAEs lie far from the AGN sequence, with their limits possibly pushing them even further, thus we conclude that the ionization in these objects is dominated by star-formation activity.

Figure 3 also compares our objects to a number of high redshift galaxies (colored shapes), as well as the low-redshift LAE analogs (gray shapes). The 4 $z \sim 2$ LBGs studied by Erb et al. (2006) are interesting, as even the ones far from the AGN sequence appear enhanced in [O III]/Hβ relative to the SDSS star-forming galaxies. This effect was also seen in lensed LBGs at similar redshifts studied by Finkelstein et al. (2009b) and Hainline et al. (2009). Examining our two objects, they appear roughly consistent with the local star-forming sequence. Further data is needed to see if this interesting trend extends to the majority of LAEs, and to diagnose its physical cause.

6. DUST EXTINCTION

One of the more intriguing results to come out of high-redshift LAE stellar population analyses is the result that many LAEs appear to have dust extinction (e.g., Pirzkal et al. 2007; Finkelstein et al. 2008, 2009c; Pentericci et al. 2009; Lai et al. 2007). This is surprising, as dust can very efficiently attenuate Lyα photons, as they resonantly scatter with neutral hydrogen, and thus can have long path lengths prior to escaping a galaxy. A number of scenarios have been discussed in the literature explaining how Lyα can escape through a dusty medium, including shifting out of resonance due to outflows (e.g., **?**Verhamme et al. 2008; **?**; **?**), as well as scattering off the surfaces of dusty H I clouds in a clumpy ISM (Neufeld 1991; Hansen & Oh 2006; Finkelstein et al. 2008, 2009c).

[5] using line fluxes from the CMU-Pitt Value-Added Catalog: http://nvogre.phyast.pitt.edu/vac/

These scenarios, or something like them, are likely in play, as observations of Lyα in local star-forming galaxies have shown that Lyα can be observed in emission even though dust is present (e.g., Atek et al. 2008), and both low- and high-redshift observations have found evidence that the Lyα emission is extended (Östlin et al. 2009; Finkelstein et al. 2010c). Nonetheless, the level of uncertainty on the dust contents in high-redshift LAEs is high, as the presence of dust has been deduced by fitting the spectral energy distributions (SEDs) of LAEs to stellar population synthesis models. These results suffer a number of degeneracies, with dust extinction topping the list, as the redding due to dust can also be explained by an older stellar population, or a higher metallicity.

Our spectroscopic results represent the first direct spectroscopic measurements of Hα and Hβ emission in high-redshift LAEs. We can use these measurements to compute the Balmer decrement, which is a measure of how much the Hα/Hβ ratio has been increased due to differential dust attenuation of the bluer line. To do this, we first need to assume an intrinsic ratio of Hα/Hβ, which we take to be 2.86, following Osterbock (1989) for the conditions in a typical H II region. Then, assuming the starburst dust extinction law of Calzetti et al. (2000), we compute the color excess due to dust emission. We found color excesses of E(B-V) = 0.20 $\pm$ 0.15 and E(B-V) = –0.65 $\pm$ 0.12 for COSMOS_156 and COSMOS_104, respectively. We note that this ignores any stellar absorption, which should be a small effect here (Rosa-González et al. 2002). Finkelstein et al. (2010a) found that a 1 Å correction to Hβ results in an uncertainty on E(B-V) of $\sim$ 0.05, much smaller than our current uncertainties. Unfortunately, due to the low-significance Hβ detections ($\leq 5\ \sigma$), the uncertainty on the extinction is high, and thus COSMOS_156 is consistent with E(B-V) $\sim$ 0 (and thus A_V = 0), as well as $A_V \sim 1$. The negative color excess for COSMOS_104 is perplexing, but similar negative values have been seen before (e.g., Atek et al. 2009), and may be indicated of Hβ scattering off of a reflection nebula within the galaxy. However, it is also possibly due to a difference in the flux calibration between the two filters. Nonetheless, we conclude that higher fidelity Hβ measurements are needed to make robust measurements of the dust extinction levels in LAEs. Blanc et al. (in prep) used the UV spectral slope to estimate the level of dust extinction in these objects. They found E(B-V) = 0.09 $\pm$ 0.05 for COSMOS_156, and E(B-V) = 0.10 $\pm$ 0.10 for COSMOS_104, in broad agreement with our Balmer decrement measurements.

We can still gain some insight into the ISMs in these objects by comparing the Hα flux to the Lyα flux from these two objects from the HETDEX pilot survey. We find that the ratio of Lyα flux to Hα flux in our objects to be less than the Case B value of 8.7, at 6.9 $\pm$ 0.5 in COSMOS_156, and 7.1 $\pm$ 1.1 in COSMOS_104[6] If the dust extinction is truly near zero in both objects, this implies that the ISM is very uniform, as only a small amount of dust is significantly reducing the flux ratio from the intrinsic Case B value. In the case of COSMOS_156, if the extinction is near the measured value of 0.8 mag, this implies an inhomogeneous ISM, as 0.8 mag of dust would attenuate Lyα significantly in a homogeneous geometry. The specific value of A_V = 0.8 mag in this object would necessitate $\tau_{Ly\alpha} < \tau_{continuum}$, implying that the Ly$\alpha$ equivalent width (EW) we observe is actually enhanced over the intrinsic value (Finkelstein et al. 2009c). However, the large uncertainties on the dust extinctions in these galaxies renders us unable to make conclusions about the ISM, other than that a full range of geometries appear possible. The result that both objects exhibit LyαH$\alpha \sim 7$ should prove useful to future surveys targeting Hα emission from LAEs.

[6] Although Lyα and Hα were obtained with two different instruments, no "slit" correction should be necessary. Lyα was obtained with an IFU and thus is the total Lyα flux, while Hα was corrected to total via the flux calibration (i.e., the standard star spectrum was scaled to match the 2MASS magnitude; see §2.3).

7. GAS-PHASE METALLICITY

Perhaps the most interesting quantity we can measure is the metallicities in these galaxies, which is extremely difficult to constrain with SED-fitting analyses. Currently, little is known about the metallicities in LAEs. The metallicities of LBGs are better known, if only for a few small samples. Perhaps the best comparison to our LAEs comes from Erb et al. (2006), who computed the metallicities of LBGs at $z \sim 2.3$ using the N2 index, which is based on the ratio of [N II]/Hα. They separated their sample into bins of stellar mass, and found that LBGs with $M_* > 10^{10}$ (comparable to the mass at L^*_{UV} at this redshift) have metallicities from $Z \sim 0.6 - 0.8\ Z_\odot$. The least massive bin, with $M_* = 2.7 \times 10^9$, only had an upper limit on its metallicity (as [N II] was undetected), of $Z < 0.35\ Z_\odot$. The metallicities of lensed LBGs (or lensed star-forming galaxies at similar redshifts) have been analyzed in a number of studies, finding a range of stellar and gas-phase metallicities from 0.25 - 0.8 $Z_\odot$ (Pettini et al. 2000; Teplitz et al. 2000; Finkelstein et al. 2009b; Quider et al. 2009, 2010; Dessauges-Zavadsky et al. 2010), with all but cB58 having $Z \geq 0.4\ Z_\odot$.

Although the presence of dust implies that LAEs are not composed of pristine gas, they may be more metal poor than LBGs as they are less evolved in their other physical properties. With our data, we can place the first direct constraints on the metallicities in high-redshift Lyα-selected galaxies, using both the N2 and O3N2 gas-phase metallicity indices of (Pettini & Pagel 2004). Given the expected strength of the [N II] emission line from the observed Hα flux, it is not surprising that these lines are undetected (as an AGN-dominated ionizing spectrum would be required). As such, we cannot measure direct metallicity values, but we can place meaningful constraints. Using the 1 σ upper limit on the [N II] flux with the N2 index we place upper limits on the gas-phase metallicities in our galaxies of $Z < 0.17\ Z_\odot$ for COSMOS_156, and $Z < 0.28\ Z_\odot$ for COSMOS_104 (2 σ upper limites are $Z < 0.25\ Z_\odot$ and $Z < 0.41\ Z_\odot$, respectively). The 1 σ upper limits from the O3N2 index are similar, with $Z < 0.17\ Z_\odot$ and $Z < 0.36\ Z_\odot$ for these two LAEs, respectively.

These constraints on the metallicities of these objects are extremely interesting. Specifically, the metallicity of COSMOS_156 is constrained to be less than all but one previously measured high-redshift galaxy. Erb et al. (2010) recently published a detailed study of the z = 2.3 BX galaxy Q2343-BX418. They found an upper limit on its metallicity from the N2 index of $Z_{N2} < 0.28\ Z_\odot$. They then used the knowledge of its low metallicity to use the lower branch of the R23 calibration, finding an R23 metallicity of Z_{R23} = 0.17 $Z_\odot$. This galaxy also has Lyα in emission, with EW_{rest} = 56 Å, with a somewhat broad profile with FWHM $\sim$ 850 km s^{-1}. The Lyα emission of COSMOS_156 has a similar width, of 770 km s^{-1}, implying further similarities between these two objects.

To place these metallicity limits in context, we compare them to the stellar masses of these galaxies (see §8 for details

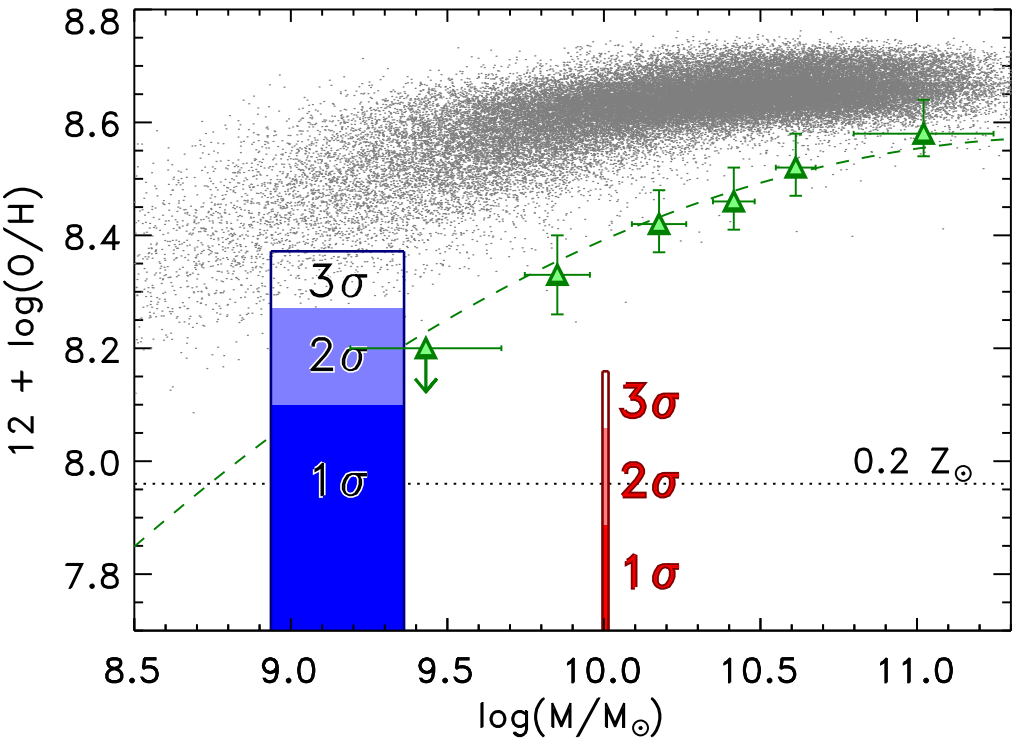

FIG. 4.— The positions of our two LAEs on a stellar mass – gas-phase-metallicity plane, using the same colors as previous plots. The small gray circles denote the SDSS sample of Tremonti et al. (2004), which represents low-redshift, star-forming galaxies, with the metallicity re-derived with the N2 index to match our objects. The green triangles denote the z $\sim$ 2.3 LBG sample of Erb et al. (2006), which comprises 87 LBGs split into six bins of stellar mass. The upper limit on the metallicity of COSMOS_156 is much lower than the $z \sim 2.3$ LBG $M-Z$ trend, even though it has $\sim L^*_{UV}$ luminosity, implying that galaxies exhibiting Lyα in emission may be systematically more metal-poor than the general galaxy population at the same redshift.

on the mass derivation). Using the emission-line corrected SED-fitting results, we find stellar masses of $10.2 \pm 0.6 \times 10^9$ $M_\odot$ and $1.6 \pm 0.7 \times 10^9$ $M_\odot$ for COSMOS_156 and COSMOS_104, respectively. Figure 4 shows these two LAEs plotted on a mass-metallicity ($M-Z$) relation. We compare their positions on this plane to those of low-redshift star-forming galaxies from the SDSS taken from Tremonti et al. (2004), as well as LBGs at $z \sim 2.3$ from Erb et al. (2006). Metallicities for the SDSS sample have been recalculated using the N2 index. LBGs at $z \sim 2.3$ lie below the low-redshift mass-metallicity sequence, though they follow the same trend, as lower-mass galaxies have lower metallicities.

Using the metallicity limits of our objects, we study high-redshift LAEs in this plane for the first time. Although COSMOS_104 is consistent with the $z \sim 2.3$ LBG $M-Z$ relation at 2 σ, its 1 σ metallicity limit lies below this relation. As we discuss below, its mass may be higher, as it is undetected in the photometry at $\lambda > 1$ μm, thus the amount of mass in old stars is unconstrained. More interesting is the position of COSMOS_156. This object has a well constrained mass, and an even lower limit on its metallicity, and we find that it lies below the $z \sim 2.3$ LBG $M-Z$ relation by at least 0.3 dex. As discussed above, SED-fitting studies have shown that LAEs are likely less evolved than LBGs in stellar mass, stellar population age and dust extinction. Here, we show for the first time evidence that LAEs may be less evolved in metallicity as well, possibly by a large amount. This is even more intriguing given the relatively large stellar mass of COSMOS_156. From the observed photometry, this galaxy's rest-frame luminosity corresponds to ~ 1.1 L* using the $z \sim 2.3$ UV luminosity function of Reddy & Steidel (2009, the luminosity of COSMOS_104 corresponds to ~ 0.5 L*). Thus, COSMOS_156 is as luminous is a typical color-selected LBG, yet it has a much lower metallicity. This implies that galaxies exhibiting Lyα in emission may be systematically more metal-poor than the general galaxy population at the same redshift, consistent with results found for a sample of low-redshift galaxies emitting in Lyα (Finkelstein et al. 2010a). However, more spectroscopic observations of high-redshift LAEs are needed before strong conclusions are possible.

8. EFFECT OF EMISSION LINES ON SED-FITTING RESULTS

With our sample of LAEs, we can for examine how the presence of strong emission lines in the rest-frame optical affects the physical properties derived from SED fitting, using the strengths of actual measured lines. To do this, we used the COSMOS Intermediate and Broad Band Photometry Catalog, released in April 2009[7]. This catalog provides the photometry performed on PSF-matched images in a 3″ aperture, as well as an aperture correction to correct to total magnitudes. For our LAEs, we used the photometry from this catalog in the following bands: CFHT u* (λ_c = 0.38 μm); Subaru B (0.45 μm), V (0.55 μm), r′ (0.63 μm), i′ (0.77 μm), z′ (0.89 μm); UKIRT J (1.25 μm) and CFHT WIRCAM K_s (2.15 μm). Additionally, deep *Spitzer Space Telescope* Infrared Array Camera (IRAC) data is available from the S-COSMOS IRAC Photometry Catalog at 3.6, 4.5, 5.8 and 8.0 μm (Sanders et al. 2007). We used

[7] http://irsa.ipac.caltech.edu/data/COSMOS/datasets.html

TABLE 3
BROADBAND PHOTOMETRY OF THE SAMPLE

Object	u^* (mag)	B (mag)	V (mag)	r' (mag)	i' (mag)	z' (mag)	J (mag)	K_s (mag)	3.6 (mag)	4.5 (mag)
COSMOS_156	24.11 (0.06)	23.92 (0.06)	24.07 (0.06)	24.10 (0.06)	24.18 (0.07)	23.90 (0.12)	22.73 (0.18)	22.66 (0.14)	22.59 (0.04)	22.69 (0.08)
COSMOS_104	25.89 (0.12)	24.93 (0.09)	25.27 (0.11)	25.39 (0.11)	25.52 (0.14)	25.47 (0.34)	< 25.17	24.00 (0.37)	< 25.76	< 25.07

NOTE. — The optical and near-infrared data is from the Cosmos Intermediate and Broadband Photometry Catalog, while the mid-infrared data is from the S-COSMOS catalog. Magnitude 1 σ errors are listen in parentheses. All magnitudes are corrected to total using the aperture corrections from their respective catalogs. When an object is detected at $< 2\ \sigma$ in a given band, we list the 1 σ upper limit. When we correct these fluxes for the measured Lyα line fluxes, we find corrected magnitudes for COSMOS_156 of $u^* = 25.31$ and B = 24.22, and for COSMOS_104 of B = 25.60. Likewise, correcting the measured K_s-band flux for the measured Hα emission, we find $K_s = 22.44$ in COSMOS_156 and $K_s = 24.29$ in COSMOS_104. While COSMOS_104 is not detected in the reddest IRAC bands, COSMOS_156 does have measured fluxes of $m_{[5.8]} = 22.23 \pm 0.23$ and $m_{[8.0]} = 22.35 \pm 0.59$ which were used in the SED fitting.

the flux from a 1.9″ aperture, using the provided aperture corrections to correct to total fluxes. COSMOS_104 was undetected in all IRAC bands, thus these fluxes were set to zero, and their 1 σ uncertainties were set to the image 1 σ depths from Sanders et al. (2007). The photometry for our sample is listed in Table 3, and 9″cutout stamps in each band are shown in Figure 5.

The photometry from these 12 bands were compared to a suite of synthetic stellar populations, using the updated (2007 version) of the models of Bruzual & Charlot (2003, hereafter CB07). Models were created over a range of metallicity ($0.005 - 2.5\ Z_\odot$), star-formation history (SFH; $\tau = 10^5 - 10^{9.6}$), age (1 Myr – $t_H[z]$) and dust extinction ($A_V = 0 - 1.6$ mag, using the extinction law of Calzetti et al. (2000)). IGM attenuation was applied via the prescription of Madau (1995). The best-fit model was found via χ^2-minimization, with the stellar mass being calculated as the weighted mean of the normalizations between the model flux and that in each detected ($\geq 2\ \sigma$) filter. Uncertainties on the derived properties were obtained via 10^3 Monte Carlo simulations, varying the object's fluxes within their uncertainties in each simulation.

The SED-fitting results are tabulated in Table 4, and the best-fit models are shown in Figure 6. We can see that these two objects appear to be very different. COSMOS_156 appears very old, near the age of the universe at z = 2.29, and is very massive, with a stellar mass of $\sim 3 \times 10^{10}\ M_\odot$. COSMOS_104 appears very young, with an age of only a few Myr, and is nearly two orders of magnitude less massive. Both objects also have very low stellar metallicity values of $\leq 0.2\ Z_\odot$, in agreement with the upper limits on their gas-phase metallicities.

However, from our observed optical and NIR spectra, it is apparent that the emission lines we have measured in these objects are very strong, and they may be adversely affecting the model results. In order to quantify this effect, we performed a second iteration of model fitting, where we corrected the broadband photometry for the observed Lyα and Hα emission-line fluxes. This was done in the following steps, following the appendix of **?**. First, we computed the ratio between the filter transmission value of λ_{line} and the maximum of the transmission function, R_T. Then, the amount of flux that the line contributes to the broadband measurement was computed as

$$f_{\nu,line} = R_T \times \frac{F_{line}}{\int T(\lambda)\frac{c}{\lambda^2}d\lambda} \quad (1)$$

, where $T(\lambda)$ is the filter transmission function. This flux was then subtracted from the catalog photometry. Due to the observed wavelength of Lyα this correction was made for both the u^* and *B*-bands for Lyα for COSMOS_156 (a 1.20 and 0.30 mag correction, respectively), while for COSMOS_104 only the B-band was corrected for Lyα (0.67 mag). The correction due to Hα was made to the K_s-band for both objects (0.17 and 0.28 mag, respectively). Additionally, we also excluded the J-band flux from the fit in COSMOS_156 (by making its uncertainty very large), as it appears to contain an excess in Figure 6, which is presumably due to strong [O II] emission, though future J-band spectroscopy is needed to be sure. The correction due to the Lyα fluxes will primarily affect the UV slope, and thus the derived dust extinction, while the correction due to Hα will change the amplitude of the $z - K_s$ color and the derived 4000 Å break, and thus the derived stellar population age.

The results from the SED-fitting iteration with the corrected broadband fluxes are also given in Table 4, and are shown in Figure 7. The corrected fit for COSMOS_104 is $\sim 3\times$ more massive, and a factor of ~ 15 older. However, the uncertainties on these properties are consistent with the uncorrected results. This is expected as this object is not well-constrained in the rest-frame optical. However, the changes to the physical properties of COSMOS_156 are more significant. Without accounting for the emission lines, this object appeared to have an age of ~ 3 Gyr. Properly accounting for the measured emission line flux reduces this drastically to ~ 100 Myr. Additionally, the stellar mass is a factor of $\sim 3\times$ lower, and the derived dust extinction is non-zero. This change can be understood when examining Figure 6 and Figure 7. The reduction in the flux of the u^* and *B*-bands results in a redder fit to the UV slope, implying a greater level of dust extinction[9]. At the same time, the lessened K_s-band flux lowers the $z' - K_s$ color, which lowers the amplitude of the 4000 Å break of the best-fit model. This, combined with the increased dust extinction, requires a much lower age to fit the observed z′ - [3.6] color. Thus, ignoring the presence of emission lines in this object would cause a drastically incorrect estimate of its age.

8.1. *Implications for Very High Redshifts*

The contributions of emission lines to the integrated fluxes of galaxies will have an even greater effect at high redshift, especially in the rest-frame optical. The amount that the emission line EWs affect the broadband photometry increases with

[9] Although SED fitting shows that COSMOS_156 appears to have $A_V \sim 0.1$ mag, this is consistent with the Balmer decrement measurement, which allows a range of $0 \lesssim A_V \lesssim 1$.

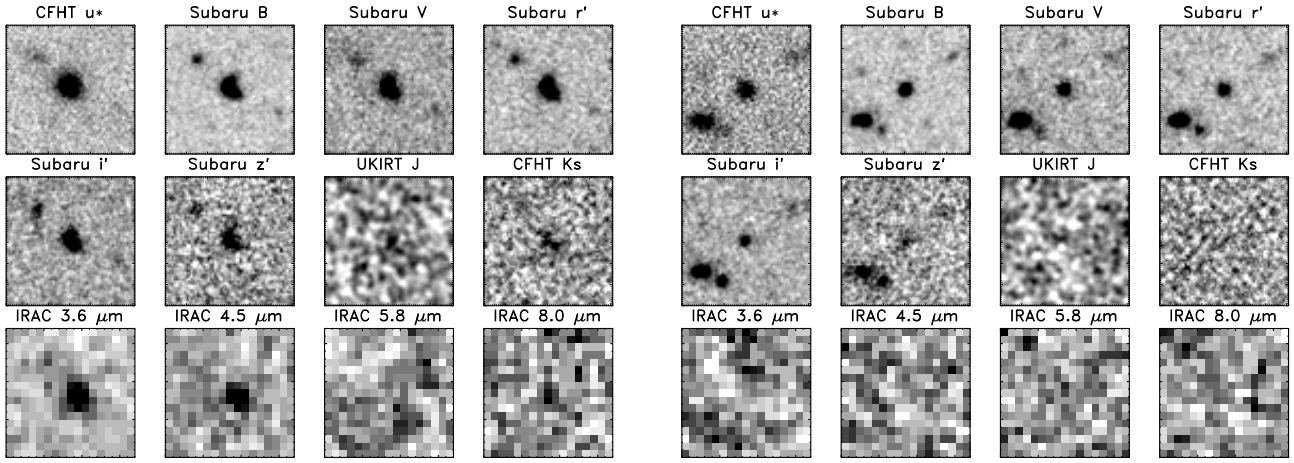

FIG. 5.— Cutout stamps of COSMOS_156 (left) and COSMOS_104 (right) in the 12 bands that were used for SED fitting, 9″ on a side. COSMOS_156 is undetected in all bands blueward of 5 μm, while COSMOS_104 is undetected in all bands redward of 1 μm.

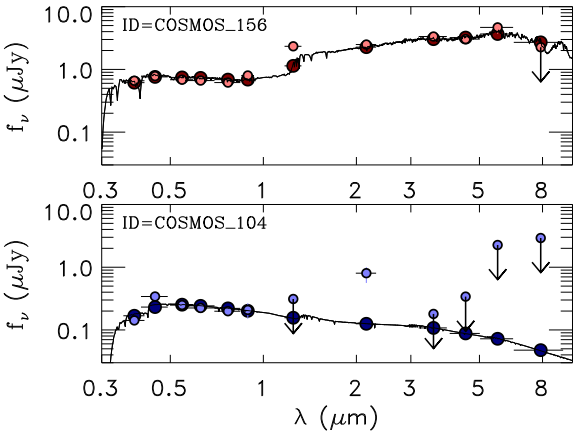

FIG. 6.— The results from performing SED-fitting on our two LAEs ignoring the presence of emission lines. The black curves are the best-fit models, the darkly-shaded circles are the bandpass-averaged fluxes of those models in the bands used for fitting, and the lightly-shaded circles are the data points. The colored lines show the 1 σ errors on the objects fluxes. For those bands that are undetected, we show the 1 σ upper limits (though the actual measured fluxes were used in the fitting).

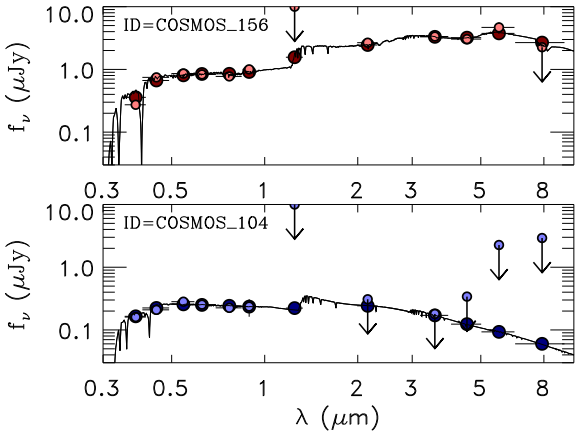

FIG. 7.— The result from SED-fitting where both the Lyα and Hα fluxes have been subtracted from the observed broadband photometry. The largest difference is apparent in COSMOS_156. A redder UV slope is allowed after the subtraction of Lyα which results in a higher derived dust extinction. Combining this with the lowered K_s-band flux results in a much younger best-fit age.

redshift, as

$$\Delta m \simeq -2.5\log\left[1+\frac{W_0(1+z)}{\Delta\lambda}\right], \qquad (2)$$

due to the increase of the observed EW with $1+z$ (or alternatively, the shrinking of the FWHM of a filter). The equivalent widths of our lines are hard to measure from the spectra alone, as in both cases the continuum is not detected, thus we cannot compute their equivalent widths. The Lyα EWs are computed by derived the continuum flux via interpolation of the flux from all detected optical filters redward of Lyα, as discussed in Adams et al. (2010, in prep). For the rest-frame optical emission lines, we use the continuum flux of the best-fit emission-line corrected model to compute the EWs, where EW = f_{line} / $f_{continuum}$, where $f_{continuum}$ is the continuum flux (in f_λ units) of the model at the wavelength of the emission line. While the continuum flux of COSMOS_156 is well-constrained at these wavelengths due to the IRAC detections, the same is not true for COSMOS_104, thus we restrict our rest-frame optical EW measurements to COSMOS_156. The rest-frame EWs are shown in Table 2. As both [N II] lines are undetected, we only list upper limits on their EWs. However, the rest-frame EWs of both [O III] lines and Hα are very strong, with EW $\sim$ 200 Å for both [O III] λ5007 and Hα.

In order to examine the effect lines of these relative strengths can have at high-redshift, we examine an example of a galaxy at z = 8 with these [O III] λ5007 and Hα EWs. At this redshift, these lines would fall in the *Spitzer* IRAC 4.5 and 5.8 μm bandpasses, which have FWHM $\approx$ 10 μm and 14 μm, respectively. These EWs thus correspond to a magnitude boost of Δm = 0.19 and 0.15 mag, respectively. While these flux increases will not result in drastic overestimates of the stellar mass, they can result in incorrect stellar population age estimates, as we have shown.

At $z \sim 7$, Labbé et al. (2009) stack a sample of 12 z-dropout galaxies, and detect the stack in both IRAC 3.6 and 4.5 μm bands. The resulting stellar population fit implies a strong 4000 Å break, due to the $H-3.6$ μm color. The galaxies that went into the stack have photometric redshifts from $\sim$ 6.5 – 7.5, thus the [O III] $\lambda\lambda$4959,5007 emission lines can contaminate the IRAC fluxes in both of these IRAC bands. The total EW of both [O III] lines measured in COSMOS_156 is $\sim$ 310 Å. Assuming that the objects are evenly distributed in redshift, this will place $\sim$ half of the line flux in each IRAC band (in reality, there are likely more objects at z $<$ 7 and

TABLE 4
DERIVED PHYSICAL PROPERTIES FROM SED FTTING

Object	Mass Best Fit ($10^9\ M_\odot$)	Mass 68% Range ($10^9\ M_\odot$)	Age Best Fit (Myr)	Age 68% Range (Myr)	A_V Best Fit (mag)	A_V 68% Range (mag)	Z Best Fit ($Z_\odot$)	Z 68% Range ($Z_\odot$)
COSMOS_156	33.60	32.77 – 34.33	3000	3000 – 3000	0.00	0.00 – 0.00	0.02	0.02 – 0.02
COSMOS_156 Corrected	9.45	9.28 – 10.55	100	100 – 100	0.08	0.08 – 0.08	0.20	0.20 – 0.20
COSMOS_104	0.38	0.22 – 0.48	1	2 – 5	0.65	0.40 – 0.73	0.02	0.02 – 0.02
COSMOS_104 Corrected	1.27	0.37 – 1.73	30	1 – 80	0.40	0.00 – 0.81	0.005	0.005 – 0.02

NOTE. — The best-fit physical properties from our SED-fitting analysis, along with the 68% confident range on each property, measured from Monte Carlo simulations. The first row for each object shows the best-fit values for the catalog photometry. The second row for each object shows the results when correcting the photometry for the measured Lyα and Hα emission lines.

at z $>$ 7, which can explain the fact that the 3.6 μm band has a brighter flux). Thus, a 150 Å emission line at $z \sim 7$ in both IRAC bands will increase the IRAC fluxes, according to Equation 1, by $\Delta m_{3.6}$ = 0.16 and $\Delta m_{4.5}$ = 0.12 mag. This reduction in the amplitude of the 4000 Å break of the best-fit model will result in a younger best-fit age. This is crucial, as Labbé et al. (2009) find a best-fit age of 300 Myr, which implies that the stars in these galaxies began forming at $z \sim 11$. In fact, including theoretical nebular emission lines in their stellar population models, Schaerer & de Barros (2010) find a best-fit age to the photometry of Labbé et al. (2009) of only 4 Myr (see also Finlator et al. 2010).

While measurements of objects in the mid-infrared at high redshift are currently very challenging, the *James Webb Space Telescope* will soon open up a wide range of high-redshift objects for SED analyses, thus the important role of emission lines needs to be accounted for to ensure accurate stellar population results.

9. CONCLUSIONS

We report on the first detections of multiple rest-frame optical emission lines from high-redshift Lyα-selected galaxies. We detected Hα, Hβ, and [O III] from two galaxies at z = 2.3 and z = 2.5, discovered with the HETDEX pilot survey. We have used these emission line measurements to directly probe the physical properties of LAEs for the first time.

Using the redshifts of the rest-frame optical emission lines as a measure of the systemic redshift, we find differences between the redshift of Lyα emission and the systemic redshift of 153 $\pm$ 37 and 31 $\pm$ 35 km s^{-1}. The slightly higher redshift of Lyα is similar to what has been seen in more evolved high-redshift galaxies, and is presumably due to a large-scale outflow in the ISMs of these galaxies. Combining our results with the only two other LAEs which have had their outflow velocities measures, we find that 3/4 of them exhibit outflows, yet all at velocities less than are typically seen in LBGs ($>$ 200 km s^{-1}). This may be due to lower star formation rates or smaller stellar masses in the LAEs, which is contrary to recent results by Steidel et al. (2010), which find that the outflow velocities are anti-correlated with the mass, thus a larger sample is needed to clearly correlate the outflow velocities in LAEs with any physical property.

Using the measured emission line flux ratios (and limits) we probe for the presence of AGN in these LAEs, using the BPT line-ratio diagnostic diagram. We find that both LAEs lie far from the AGN sequence, consistent with results at higher redshift that the AGN fraction in LAEs is very low. We use the measured Hα and Hβ lines in our objects to measure the dust extinction. However, as the detection significance of Hβ in both objects is $\lesssim 5\ \sigma$, the uncertainties on the derived extinctions are high, thus we cannot definitively rule out zero dust in these objects. However, the measured ratio of Lyα/Hα in both objects is ~ 6, thus some dust is likely causing deviation from the Case B ratio of 8.7, though the geometry of such an ISM is as yet unconstrained.

Lacking AGN contamination, we can also use the emission line ratios to measure the gas-phase metallicities. As the [N II] line is undetected in both objects, we can only place upper limits on their metallicities, which we find to be $<$ 0.28 and $<$ 0.44 $Z_\odot$ for COSMOS_156 and COSMOS_104, respectively. Combining these limits with the stellar masses measured from emission-line corrected SED-fitting results, we find that at least one of these objects lies well below the mass-metallicity sequence for LBGs at similar redshifts, implying that objects selected on the basis of their Lyα emission, even if they are relatively massive, are more metal poor than the general galaxy population at high redshift.

Lastly, we examine the results of SED fitting with and without correcting for the presence of Lyα and Hα emission lines. We find that ignoring this strong line emission results in an overestimation of the age by orders of magnitude, and an overestimation of the stellar mass by a factor of three. This is highly significant for high-redshift studies, as we find that the rest-frame EWs of both [O III] and Hα are $\sim$ 200 Å, and since the amount with which the emission line affects a broadband flux is proportional to $1+z$, correcting for this contamination is crucial at high redshift.

Near-infrared spectroscopy allows us to probe the physical characteristics of high-redshift galaxies with a much higher precision than is possible with SED-fitting techniques alone. Although it is currently time expensive, the presence of multi-object NIR spectrographs will alleviate this in the near future. Additionally, the ability of the *James Webb Space Telescope* to take mid-infrared spectroscopy will allow these analyses to be pushed to higher redshifts very soon.

REFERENCES

Atek, H., Kunth, D., Hayes, M., Östlin, G., & Mas-Hesse, J. M. 2008, A&A, 488, 491

Atek, H., Kunth, D., Schaerer, D., Hayes, M., Deharveng, J. M., Östlin, G., & Mas-Hesse, J. M. 2009, A&A, 506, L1

Baldwin, J. A., Phillips, M. M., & Terlevich, R. 1981, PASP, 93, 5

Bruzual, G., & Charlot, S. 2003, MNRAS, 344, 1000
Calzetti, D., Armus, L., Bohlin, R. C., Kinney, A. L., Koornneef, J., & Storchi-Bergmann, T. 2000, ApJ, 533, 682
Cowie, L. L., & Hu, E. M. 1998, AJ, 115, 1319
Deharveng, J.-M., et al. 2008, ApJ, 680, 1072
Dessauges-Zavadsky, M., D'Odorico, S., Schaerer, D., Modigliani, A., Tapken, C., & Vernet, J. 2010, A&A, 510, A26+
Erb, D. K., Pettini, M., Shapley, A. E., Steidel, C. C., Law, D. R., & Reddy, N. A. 2010, ApJ, 719, 1168
Erb, D. K., Steidel, C. C., Shapley, A. E., Pettini, M., Reddy, N. A., & Adelberger, K. L. 2006, ApJ, 646, 107
Eyles, L. P., Bunker, A. J., Ellis, R. S., Lacy, M., Stanway, E. R., Stark, D. P., & Chiu, K. 2007, MNRAS, 374, 910
Eyles, L. P., Bunker, A. J., Stanway, E. R., Lacy, M., Ellis, R. S., & Doherty, M. 2005, MNRAS, 364, 443
Finkelstein, S. L., Cohen, S. H., Malhotra, S., Rhoads, J. E., & Papovich, C. 2010a, ApJ Submitted
Finkelstein, S. L., Cohen, S. H., Malhotra, S., Rhoads, J. E., Papovich, C., Zheng, Z. Y., & Wang, J. 2009a, ApJ, 703, L162
Finkelstein, S. L., Papovich, C., Giavalisco, M., Reddy, N. A., Ferguson, H. C., Koekemoer, A. M., & Dickinson, M. 2010b, ApJ, 719, 1250
Finkelstein, S. L., Papovich, C., Rudnick, G., Egami, E., Le Floc'h, E., Rieke, M. J., Rigby, J. R., & Willmer, C. N. A. 2009b, ApJ, 700, 376
Finkelstein, S. L., Rhoads, J. E., Malhotra, S., & Grogin, N. 2009c, ApJ, 691, 465
Finkelstein, S. L., Rhoads, J. E., Malhotra, S., Grogin, N., & Wang, J. 2008, ApJ, 678, 655
Finkelstein, S. L., Rhoads, J. E., Malhotra, S., Pirzkal, N., & Wang, J. 2007, ApJ, 660, 1023
Finkelstein, S. L., et al. 2010c, ArXiv e-prints, astroph/1008.0634
Finlator, K., Oppenheimer, B. D., & Davé, R. 2010, ArXiv e-prints
Fontana, A., et al. 2006, A&A, 459, 745
Gawiser, E., et al. 2006, ApJ, 642, L13
—. 2007, ApJ, 671, 278
González, V., Labbé, I., Bouwens, R. J., Illingworth, G., Franx, M., Kriek, M., & Brammer, G. B. 2010, ApJ, 713, 115
Gronwall, C., et al. 2007, ApJ, 667, 79
Hainline, K. N., Shapley, A. E., Kornei, K. A., Pettini, M., Buckley-Geer, E., Allam, S. S., & Tucker, D. L. 2009, ApJ, 701, 52
Hansen, M., & Oh, S. P. 2006, MNRAS, 367, 979
Hayes, M., et al. 2010, Nature, 464, 562
Hill, G. J., et al. 2008, in Astronomical Society of the Pacific Conference Series, Vol. 399, Astronomical Society of the Pacific Conference Series, ed. T. Kodama, T. Yamada, & K. Aoki, 115–+
Huang, J., et al. 2007, ApJ, 660, L69
Kauffmann, G., et al. 2003, MNRAS, 346, 1055
Kewley, L. J., Dopita, M. A., Sutherland, R. S., Heisler, C. A., & Trevena, J. 2001, ApJ, 556, 121
Labbé, I., et al. 2009, ArXiv e-prints, 0910.0838
Lai, K., Huang, J.-S., Fazio, G., Cowie, L. L., Hu, E. M., & Kakazu, Y. 2007, ApJ, 655, 704
Lai, K., et al. 2008, ApJ, 674, 70
Madau, P. 1995, ApJ, 441, 18
Malhotra, S., Wang, J. X., Rhoads, J. E., Heckman, T. M., & Norman, C. A. 2003, ApJ, 585, L25
Martin, C. L. 2005, ApJ, 621, 227
McLean, I. S., et al. 1998, in Presented at the Society of Photo-Optical Instrumentation Engineers (SPIE) Conference, Vol. 3354, Society of Photo-Optical Instrumentation Engineers (SPIE) Conference Series, ed. A. M. Fowler, 566–578
McLinden, E. M., et al. 2010, ArXiv e-prints, astroph/1006.1895
Neufeld, D. A. 1991, ApJ, 370, L85
Oke, J. B., & Gunn, J. E. 1983, ApJ, 266, 713
Ono, Y., Ouchi, M., Shimasaku, K., Dunlop, J., Farrah, D., McLure, R., & Okamura, S. 2010a, ArXiv e-prints
Ono, Y., et al. 2010b, MNRAS, 402, 1580
Osterbock, D. E. 1989, Astrophysics of Gaseous Nebulae and Active Galactic Nuclei (Mill Valley: University Science Books)
Östlin, G., Hayes, M., Kunth, D., Mas-Hesse, J. M., Leitherer, C., Petrosian, A., & Atek, H. 2009, AJ, 138, 923
Ouchi, M., et al. 2008, ApJS, 176, 301
—. 2009, ApJ, 706, 1136
Overzier, R. A., et al. 2009, ApJ, 704, 548
Papovich, C., Dickinson, M., & Ferguson, H. C. 2001, ApJ, 559, 620
Pentericci, L., Grazian, A., Fontana, A., Castellano, M., Giallongo, E., Salimbeni, S., & Santini, P. 2009, A&A, 494, 553
Pettini, M., & Pagel, B. E. J. 2004, MNRAS, 348, L59
Pettini, M., Steidel, C. C., Adelberger, K. L., Dickinson, M., & Giavalisco, M. 2000, ApJ, 528, 96
Pirzkal, N., Malhotra, S., Rhoads, J. E., & Xu, C. 2007, ApJ, 667, 49
Puccetti, S., et al. 2009, ApJS, 185, 586
Quider, A. M., Pettini, M., Shapley, A. E., & Steidel, C. C. 2009, MNRAS, 398, 1263
Quider, A. M., Shapley, A. E., Pettini, M., Steidel, C. C., & Stark, D. P. 2010, MNRAS, 402, 1467
Reddy, N. A., & Steidel, C. C. 2009, ApJ, 692, 778
Reddy, N. A., Steidel, C. C., Erb, D. K., Shapley, A. E., & Pettini, M. 2006, ApJ, 653, 1004
Rhoads, J. E., Malhotra, S., Dey, A., Stern, D., Spinrad, H., & Jannuzi, B. T. 2000, ApJ, 545, L85
Rosa-González, D., Terlevich, E., & Terlevich, R. 2002, MNRAS, 332, 283
Rupke, D. S., Veilleux, S., & Sanders, D. B. 2005, ApJS, 160, 115
Sanders, D. B., et al. 2007, ApJS, 172, 86
Sawicki, M., & Yee, H. K. C. 1998, AJ, 115, 1329
Schaerer, D., & de Barros, S. 2010, A&A, 515, A73+
Shapley, A. E., Steidel, C. C., Adelberger, K. L., Dickinson, M., Giavalisco, M., & Pettini, M. 2001, ApJ, 562, 95
Shapley, A. E., Steidel, C. C., Erb, D. K., Reddy, N. A., Adelberger, K. L., Pettini, M., Barmby, P., & Huang, J. 2005, ApJ, 626, 698
Shapley, A. E., Steidel, C. C., Pettini, M., & Adelberger, K. L. 2003, ApJ, 588, 65
Stark, D. P., Ellis, R. S., Bunker, A., Bundy, K., Targett, T., Benson, A., & Lacy, M. 2009, ApJ, 697, 1493
Steidel, C. C., Erb, D. K., Shapley, A. E., Pettini, M., Reddy, N., Bogosavljević, M., Rudie, G. C., & Rakic, O. 2010, ApJ, 717, 289
Steidel, C. C., & Hamilton, D. 1993, AJ, 105, 2017
Stern, D., et al. 2005, ApJ, 631, 163
Teplitz, H. I., et al. 2000, ApJ, 533, L65
Tremonti, C. A., et al. 2004, ApJ, 613, 898
van Dokkum, P. G. 2001, PASP, 113, 1420
Verhamme, A., Schaerer, D., Atek, H., & Tapken, C. 2008, A&A, 491, 89
Wang, J. X., et al. 2004, ApJ, 608, L21
Yan, H., Dickinson, M., Giavalisco, M., Stern, D., Eisenhardt, P. R. M., & Ferguson, H. C. 2006, ApJ, 651, 24
Yan, H., et al. 2005, ApJ, 634, 109
Yuma, S., Ohta, K., Yabe, K., Shimasaku, K., Yoshida, M., Ouchi, M., Iwata, I., & Sawicki, M. 2010, ApJ, 720, 1016